Spatial Properties of High-Order Harmonic Beams from Plasma Mirrors: A Ptychographic Study

A. Leblanc, S. Monchocé, H. Vincenti, S. Kahaly, J.-L. Vay, and F. Quéré

Spatial properties of high-order harmonic beams from plasma mirrors: a ptychographic study

A. Leblanc,[1] S. Monchocé,[1] H. Vincenti,[1, 2] S. Kahaly,[1] J-L. Vay,[2] and F.Quéré[1]

[1]*LIDYL, CEA, CNRS, Université Paris-Saclay, CEA Saclay, 91 191 Gif-sur-Yvette, France*
[2]*Lawrence Berkeley National Laboratory, Berkeley, CA 94720, USA*
(Dated: June 30, 2017)

Spatial properties of high-order harmonic beams produced by high-intensity laser-matter interactions carry rich information on the physics of the generation process, and their detailed understanding is essential for applications of these light beams. We present a thorough study of these properties in the case of harmonic generation from plasma mirrors, up to the relativistic interaction regime. In-situ ptychographic measurements of the amplitude and phase spatial profiles of the different harmonic orders in the target plane are presented, as a function of the key interaction parameters. These measurements are used to validate analytical models of the harmonic spatial phase in different generation regimes, and to benchmark ultrahigh-order Maxwell solvers of Particle-In-Cell simulation codes.

Plasma mirrors are dense plasmas produced at the surface of solid targets when these are ionized by intense femtosecond (fs) laser pulses [1]. Due to their solid-like density ($\approx 10^{23} \ cm^{-3}$) and to the very limited expansion of the plasma into the vacuum on femtosecond time scale, they specularly reflect these intense laser pulses, just like ordinary mirrors do for low-intensity laser beams. Plasma mirrors can therefore be used as single-shot optical devices for the manipulation of intense fs laser beams [1–5]. At high enough intensities ($\gtrsim 10^{16} \ W/cm^2$), the response of the plasma to the field becomes highly non-linear, and the waveform of the laser field gets periodically distorted upon reflection [1, 6]. This results in the generation of high-order harmonics (HH) [7, 8] of the laser frequency, associated in the time domain with trains of intense [9] attosecond light pulses.

The generated high harmonic phase and amplitude profiles are very sensitive to the laser [11–14] and plasma characteristics [15–19]. Understanding the properties of these extreme ultraviolet (XUV) radiation sources and their relation to the laser and plasma parameters is thus essential for predictive control and subsequent applications in attoscience experiments [20, 21]. These necessitate at first step to be able to fully characterize the temporal [22, 23] and spatial properties of the harmonics, which are very challenging to measure due to extreme physical conditions.

The harmonic beam characteristics are encoded in their spatial features at birth [11, 13, 14, 24] and a clear insight would not only allow development of suitable beam propagation techniques [25] but would also enable their synthesis with powerful approaches like the attosecond lighthouse scheme for the generation of isolated attopulses [26, 27]. The major goal of HH spatial metrology is to understand two properties of the harmonic source, its spatial extent and spatial curvature, which were not simultaneously available until now: one had to be assumed in order to deduce the other [11, 13, 14, 24].

In this letter, we use the recently-developed technique of in-situ ptychography [28] to measure the spatial amplitude and phase profiles $|E_n(\mathbf{r})|$ and $\varphi_n(\mathbf{r})$ of harmonic sources produced from plasma mirrors as a function of the most relevant interaction parameters [16]. The study spanning over two orders of magnitude in laser intensity and one order of magnitude in plasma density scale length accesses the two most dominant mechanisms of HH from plasma mirrors in this regime: Coherent Wake Emission (CWE) and the Relativistic Oscillating Mirror (ROM) process [7, 8]. The results provide insight into the collective dynamics of electrons at plasma surfaces driven by ultraintense laser fields. The accurate and comprehensive information obtained on the harmonic spatial properties enable us to validate analytical models [13, 14] of the harmonic phase and benchmark numerical schemes [29–31] used to describe nonlinear laser-plasma interaction. All these are essential for future applications of these beams.

Defining $E_n(\mathbf{r}) = |E_n(\mathbf{r})| \exp[i\varphi_n(\mathbf{r})]$ as the complex field of the nth harmonic *right at the output of the generation medium* (with $\mathbf{r}$ the 2D position vector transverse to the propagation direction), the field far away from the source is determined by the spatial Fourier transform $\tilde{E}_n(\mathbf{k})$ of $E_n(\mathbf{r})$. The divergence θ_n of this harmonic beam is related to the width Δk of $|\tilde{E}_n(\mathbf{k})|^2$, through $\theta_n \propto \Delta k/k_n$ (with $k_n = 2\pi/\lambda_n$ the nth harmonic wavevector). This width is imposed by two factors, both intimately linked to the physics of the harmonic generation process.

The first one is the spatial extent of $|E_n(\mathbf{r})|$, which defines the size w_n of the harmonic source. This source size is typically a fraction of the laser focal spot size w_L, due to the intrinsic non-linearity of the generation mechanism. The second key quantity is the harmonic spatial phase $\varphi_n(\mathbf{r})$. It originates from the dependence of the harmonic phase on the laser field amplitude, $\varphi_n(\mathbf{r}) = \varphi_n[a(\mathbf{r})]$ ($a(\mathbf{r})$ normalized laser vector potential at transverse position $\mathbf{r}$ in the interaction plane). This dependence is dictated by the laser-driven dynam-

ics of the physical system (e.g. plasma mirrors, atomic or molecular gases) involved in the harmonic generation. In all generation processes discovered until now, this spatial phase has been found to have a major impact on the beam divergence [11, 12, 32].

We first briefly introduce the CWE and ROM mechanisms, discuss the origins of the spatial phase $\varphi_n(\mathbf{r})$ of the associated harmonic sources, and use existing analytical models to present the main features of these phases. We start with CWE [33], which is typically dominant for $a \leq 1$ and sharp density gradients $L \lesssim \lambda/20$ [16] (with L the scale length of the density gradient at the plasma surface, which characterizes the steepness of the plasma-vacuum interface). In this regime, attosecond pulses are emitted by collective electronic plasma oscillations excited within the overdense part of the density gradient (see density map in Fig.1a and its inset). These plasma oscillations are triggered once every optical period by electronic density peaks, formed by the crossing of trajectories (i.e. a caustic) of fast electrons injected from the plasma surface towards the bulk by the incident laser field (so-called Brunel electrons [34]). The higher the laser field strength, the larger the effective propagation velocity of this caustic inside the plasma, and the earlier the attosecond pulses are emitted within the laser optical cycle -an effect described by an intensity-dependent emission time $\tau_e(a)$ [12, 13].

An analytical expression of $\tau_e(a)$ has been derived in [13], by calculating the shape of the caustic formed by electron trajectories. Using this expression, and a Taylor expansion of $a(\mathbf{r}) = a_0 \exp(-r^2/w_L^2) \approx a_0(1 - r^2/w_L^2)$ around the center of the focal spot, we find [41] that the spatial phase of CWE harmonics is $\varphi_n(\mathbf{r}) = \omega_n \tau_e[a(\mathbf{r})] = k_n r^2/2R$, with the wavefront curvature $1/R$ given by:

$$\frac{w_L^2}{\lambda_L R} = -\eta \left[\frac{L}{\lambda_L} \times \frac{1}{a_0} \right]^{1/3} \tag{1}$$

where $\eta = 1.45/3 \times \left(2\ln(n/\cos\theta)/\sin\theta \right)^{1/3}$, λ_L is the laser wavelength, and θ the incidence angle on target. Note that the dependence on harmonic order n (through η) is very weak and can be neglected in practice. This curvature of the attosecond beam wavefronts right after the target is clearly observed in the simulation results of Fig.1a. As attosecond pulses are emitted earlier near the center of the focal spot than on the edges (where the caustic velocity is lower), the harmonic beam has diverging wavefronts in the source plane (Fig.1a). The curvature $1/R$ is plotted in Fig.1b as a function of the two key physical parameters of the interaction, a_0, the peak amplitude of the laser field at the center of the focal spot, and L. The larger L, or the lower a_0, the stronger the curvature, because the variation of $\tau_e[a(\mathbf{r})] \propto (L/a_0)^{1/3}$ across the focal spot gets larger in magnitude, as Brunel electrons need on average more time to go from the critical density
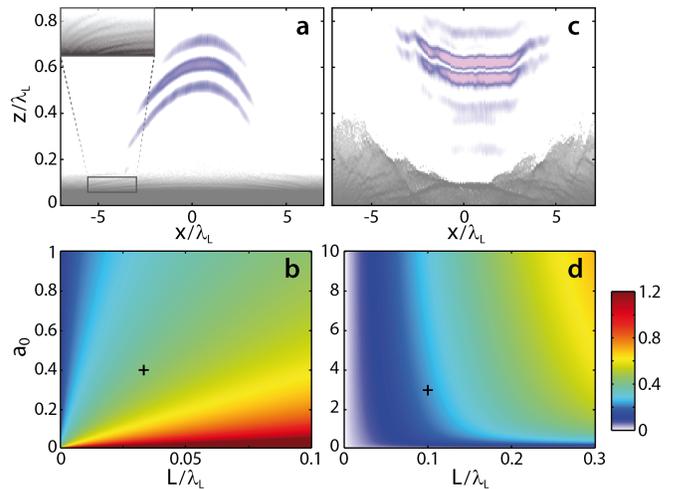
FIG. 1. Spatial properties of high-order harmonics and attosecond pulses. Panels a and c show results of 2D Particle-in-Cell simulations, respectively in the CWE ($a_0 = 0.4$, $L = \lambda_L/30$) and ROM ($a_0 = 3$, $L = \lambda_L/10$) generation regimes, plotted here in a Lorentz frame [35] where the laser field is normally incident on the plasma ($\theta = 45^o$ in the laboratory frame). The gray scale map shows the plasma electron density at a given time in a laser optical cycle. The color map shows the wavefronts of a single attosecond pulse (harmonics 4 to 12), emitted during the same cycle but plotted at a slightly later time, after it has propagated in vacuum. Panels b and d show the absolute value of the wavefront curvature $1/R$ (in units of λ_L/w_L^2) of the harmonic beam for these two generation mechanisms, predicted by analytical models (Eqs. 1 and 2), as a function of a_0 and L. The black crosses indicate the physical conditions used in panels a and c.

surface to the dense part of the plasma.

The second mechanism is the ROM process, which generally dominates for $a \geq 1$ and longer density gradients $L \gtrsim \lambda/20$ [16]. In this case, attosecond pulses result from the periodic Doppler upshift induced on the reflected laser waveform by the laser-driven relativistic oscillation of the plasma mirror surface. At these much higher intensities, the time-averaged Lorentz force exerted by the laser on the plasma mirror can make its surface drift inwards by a fraction of the laser wavelength. As the laser intensity is in most cases spatially non-uniform on target, this displacement δx varies across the irradiated spot, thus creating a concave emitting plasma surface [11]. This effect is clearly observed on the plasma density distribution (Fig.1c), and has been modeled and calculated analytically in [14]. This in turn results in a temporal delay $\tau_e(\mathbf{r}) = 2\cos\theta \delta x(\mathbf{r})/c$ on the emission of ROM attosecond pulses, associated to a spatial phase $\varphi_n(\mathbf{r}) = \omega_n \tau_e(\mathbf{r})$ of the nth harmonic, which now corresponds to converging wavefronts (Fig.1c) -i.e. the attosecond pulses get focused in front of the plasma surface. Using the same Taylor expansion of $a(\mathbf{r})$ as before, this phase is given by $\varphi_n(r) = k_n r^2/2R$, with $1/R$ the curvature of the harmonic wavefront, identical for all harmonic

orders [41]:

$$\frac{w_L^2}{\lambda_L R} = 4\cos\theta \times a_0 \times \frac{L}{\lambda_L} \times \frac{2\alpha(1+\alpha a_0)+\beta}{(1+\alpha a_0)^2+\beta a_0} \qquad (2)$$

with α and β two parameters depending on L and θ, respectively associated to the plasma ion and electron dynamics. Like in the CWE case, this curvature of the attosecond beam wavefronts right after the target is observed on the simulations results of Fig.1c.

This curvature is plotted in Fig.1d, as a function of a_0 and L. It again increases with L, because a softer plasma gradient is more easily deformed by the incident field. It always tends to increase with a_0, but this dependence gets weak as soon as $a_0 > 4 - 5$. From Eq.2, this is because $1/R \rightarrow 4L/w_L^2$ when $a_0 \gg 1/\alpha, \beta/\alpha^2$. Note that for both CWE and ROM, the wavefront radius of curvature R scales as w_L^2/λ_L ($\approx 20~\mu m$ for $w_L = 4~\mu m$ and $\lambda_L = 0.8~\mu m$), and tends to be smaller from CWE (stronger curvature) than for ROM [12], as observed in Fig.1 b,d.

This shows how the wavefront curvature $1/R$ of harmonic beams *in the source plane* is directly related to the dynamics of the plasma in the ultraintense laser field. Accessing this phase profile experimentally is however very challenging. Measurements of the harmonic beam amplitude and phase profiles *far away from the target* are possible [36, 37], but deducing the phase profile in the source plane would then require the knowledge of the propagation distance from the source to the measurement plane with sub-100 μm accuracy, which would be extremely challenging in practice. $\varphi_n(\mathbf{r})$ can be inferred from measurements of the harmonic beam divergence in the far field [14], but only with the use of additional information on the source size w_n (e.g. obtained from simulations). At present, phase-retrieval techniques constitute the only accurate way to access the harmonic wavefront curvature *in the target plane*. Here, we use the measurement technique demonstrated in [28], which is a particular case of the lensless imaging method called ptychography.

This technique consists in measuring the diffraction patterns $I(\mathbf{k}, \mathbf{r}_0)$ produced by a probe beam $E(\mathbf{r})$ diffracted out by an object $O(\mathbf{r})$, for different relative positions $\mathbf{r}_0$ between the probe and object. Phase-retrieval algorithms enable the complete reconstruction, in amplitude and phase, of both the object and the probe spatial profiles from this set of data [38, 39]. It has recently been adapted to the spatial characterization of harmonics beams from plasma mirrors [28], by generating these harmonics on a spatially-modulated plasma mirror surface that acts as the object $O(\mathbf{r})$. This harmonic beam thus constitutes the probe $E(\mathbf{r})$, which is here directly generated on the object, instead of being provided by an external source as in usual ptychography. The modulated plasma mirror surface can be obtained in-situ by optically microstructuring an initially flat solid target,

using a combination of two interfering prepulse beams to trigger a spatially-modulated plasma expansion [40]. The diffraction pattern produced by this modulated plasma surface is measured as a function of $\mathbf{r}_0$ for each harmonic order, using an angularly-resolved XUV spectrometer [41]. A single experimental scan of $\mathbf{r}_0$ thus simultaneously provides one ptychographic dataset for each observable harmonic order. All measurements presented below have been performed with the UHI100 laser, the 100 TW-25 fs high-contrast Ti-Sapphire laser of CEA Saclay.

Two typical phychographic datasets measured for the 12th harmonic, each consisting of ≈ 100 laser shots, are displayed in Fig.2a and 2b, respectively in the CWE and ROM generation regimes. The spatial amplitude and phase profiles of the harmonic source in the target plane are then reconstructed by applying a phase-retrieval algorithm to these datasets and displayed in panels c and d for four different harmonic orders [41]. From these profiles, the two parameters that determine the harmonic beam divergence, the source size w_n and the wavefront curvature $1/R$, can be obtained as a function of harmonic order. These are plotted in panels e-g for CWE and f-h for ROM (red and orange dots), for all harmonic orders observed in these scans.

The harmonic source size w_n is close to the laser focal spot size ($\approx 75\%$) in the case of CWE, and only weakly varies with harmonic order, except for the highest order. This is due to the weak dependence of the harmonic generation efficiency on laser intensity, i.e. to the weak non-linearity of this generation process [8, 33]. In contrast, the source size of ROM harmonics is a small fraction ($\lesssim 30\%$ for 11th order) of the laser source size, and decreases with harmonic order down to $\approx 12\%$ for the 26th harmonic. This is consistent with the stronger non-linearity of this generation mechanism, especially in this range of laser field amplitude [8], close to the onset where ROM starts coming into play. Another striking feature is the strong difference in the shapes $|E_n(\mathbf{r})|$ of these two types of sources: while the ROM sources preserve the quasi-Gaussian shape of the laser focus, the CWE sources display super-Gaussian profiles, which might indicate a saturation of the generation mechanism around the center of the laser focus.

These results are compared to the source sizes derived from 2D PIC simulations performed with the code WARP+PXR [29, 30] in these two generation regimes. Two types of Maxwell solvers have been used for these simulations: a standard second-order Yee solver [42] (grey curves), and a recently developed ultrahigh-order spectral solver [31] (black curves) that greatly reduces numerical dispersion of electromagnetic waves as well as numerical noise. In the CWE regime, the results obtained with the spectral solver agree very well the experimental results (including the sudden reduction in source size observed for the last harmonic order), while this is not the case at all for those obtained with the Yee solver, due
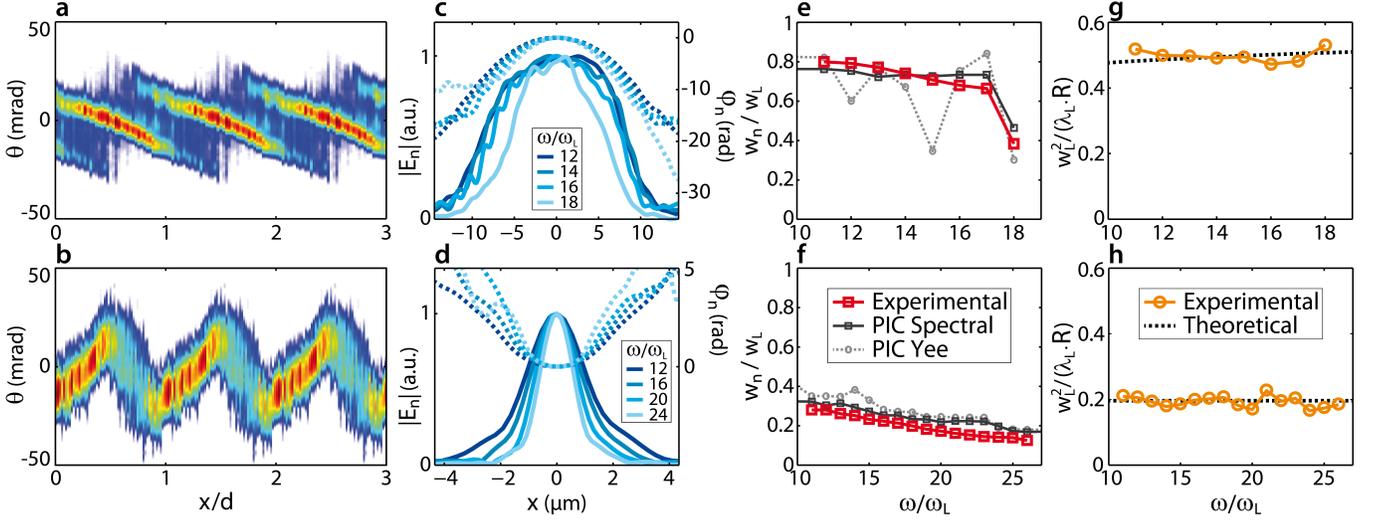
FIG. 2. Typical ptychographic measurements of harmonic beams produced by plasma mirrors. Panel a and b show ptychographic datasets measured for the 12th harmonic, in the CWE ($a_0 = 0.2$, $L = \lambda_L/35$) and ROM ($a_0 = 1.65$, $L = \lambda/8$) generation regimes. d is the spatial period of the transient plasma grating used for the measurement. The amplitude (full lines) and phase (dashed lines) spatial profiles of the harmonic source retrieved from such measurements are shown in panel c and d, for four harmonic orders in each case. The harmonic source size w_n (red plot, in units of laser focal spot size w_0) and the wavefront radius of curvature $|1/R|$ (orange plot, in units of λ_L/w_0^2) are respectively displayed in panels e-f and g-h, for all harmonic orders observable in these scans. The source sizes obtained from 2D PIC simulations in the same interaction conditions as these experiments are shown in panels e-f, in the cases of a second-order Yee solver (grey plot) and a ultrahigh-order (order=128 was used here) spectral solver (black plot) for Maxwell's equations. The dashed lines in g-h correspond to the predictions of Eq.1 and 2.

to the much stronger numerical noise. These measurements thus provide a stringent test of the performances of Particle-In-Cell simulation codes. In the ROM regime, for both solvers, the numerical results properly reproduce the evolution of the source size with harmonic order, although they provide values that are slightly larger than the experimental results, by about 10% at the lowest harmonic orders for the spectral solver, and about twice more for the Yee solver.

The phase profiles presented in Fig.2c-d provide a direct confirmation of the very contrasted properties of CWE and ROM harmonic beams. Clear phase curvatures are observed in both cases, which are of opposite signs for these two mechanisms, as expected from the physics of the generation. The magnitude of the harmonic spatial phase increases with harmonic order in both cases, but tends to be larger for CWE than for ROM. By fitting the central part of $\varphi_n(\mathbf{r})$ by a second-order polynomial $k_n r^2/2R_n$ [41], we extract a measured wavefront curvature $1/R_n$ for each harmonic order, plotted in orange in Fig.2g-h. This wavefront curvature is found to be quasi-independent of harmonic order, $1/R_n = 1/R$, thus validating a key physical prediction of both previously described theoretical models.

We studied the evolution of this 'effective surface curvature' $1/R$ by performing several ptychographic measurements for different values of a_0 (varied using an attenuator) and L (varied by changing the delay between the two prepulses and the main pulse) [41]. For each of

these measurements, we applied the same data processing as in the case of Fig.2, and obtained a curvature $1/R_n$ that was in all cases found to be independent of harmonic order [41], $1/R_n = 1/R$, as in Fig.2g-h. The results of this parametric study are shown as dots in Fig.3 for the ROM and CWE mechanisms. The multiple evaluations of $1/R$ obtained from a single ptychographic scan (between 8 and 16, i.e. one for each measured harmonic order, see Fig.2g-h) allows calculation of the error bars in Fig.3.

Figure 3 also compares these experimental results to the predictions of the analytical models of the phase curvature (Eq.1 and Eq.2), shown as full lines. These theoretical predictions require the determination of two sets of parameters $(a_0, L)_i$ corresponding to the experimental points. This is achieved based on the relative variations of these two parameters, which are known with a good accuracy since they are directly determined by well-controlled experimental parameters [41]. With this procedure, our measurements provide a very stringent test of the *evolution* of $1/R$ with these interaction parameters, which validates the analytical models of the effective surface curvature.

In conclusion, we have presented an advanced metrology study of ultrahigh-intensity laser-plasma interactions, incorporating $\sim 10^4$ measurements (Fig.3), which unravels the contrasting amplitude and phase behaviour of CWE and ROM mechanisms (Fig.2). Enabling experimental access to the properties of the harmonic beams
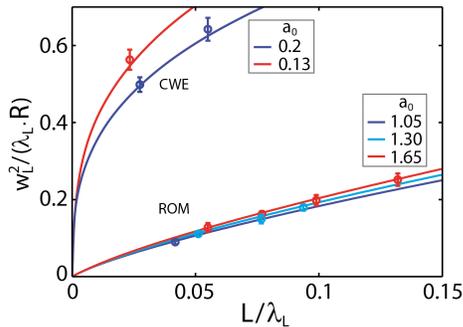
FIG. 3. Measured curvatures $|1/R|$ of the harmonic wavefronts in the CWE and ROM regimes, as a function of the laser amplitude a_0 and the density gradient scale length L. These points are the results of $\approx 11 \times 100 = 1100$ laser shots, which provide ≈ 13000 independent harmonic angular profiles (one for each harmonic order in each laser shot) used in the ptychographic analysis. The full lines show the predictions of the analytical models (Eq.1 and Eq.2).

right in the target plane, it provides firm validation of analytical models for the phase properties of high-order harmonic beams produced from plasma mirrors, both in the non-relativistic and relativistic regimes, and a benchmark for simulation codes. The measurements have direct relevance to new powerful techniques like two color relativistic control at attosecond time scales [43] and can easily be extended to the few cycle regime [5, 44, 45]. These models will be essential for the optimization of future light sources based on this type of interaction. Complete analytical formulations of the spatial properties would need predictive models of the harmonic source size w_n for both CWE and ROM that is still a great challenge requiring dependence of the generation efficiency on laser intensity. This calls for quantitative models of the entire harmonic generation process, that are still missing today. The work presented here is a step forward towards this ambitious goal.

[1] C. Thaury *et al.*, Nature Physics **3**, 424 (2007).
[2] G. Doumy *et al.*, Physical Review E **69**, 026402 (2004).
[3] R. Hoerlein *et al.*, New Journal of Physics **10**, 083002 (2008).
[4] M. Nakatsutsumi *et al.*, Optics Letters **35**, 2314 (2010).
[5] J. Wheeler *et al.*, Nature Photonics **6**, 829 (2012).
[6] B. Dromey, *et al* Nature Physics **2**, 456 (2006).
[7] U. Teubner and P. Gibbon, Rev. Mod. Phys. **81**, 445 (2009).
[8] C. Thaury and F. Quéré, J. Phys. B. **43**, 213001 (2010).
[9] G. Sansone, *et al* Nat. Photonics **5**, 655 (2011).
[10] M. Thévenet *et al.*, Nature Physics **12**, 355 (2016), 1511.05936.
[11] B. Dromey, *et al* Nat. Phys. **5**, 146 (2009).
[12] F. Quéré *et al.*, Physical Review Letters **100**, 095004 (2008).
[13] A. Malvache, A. Borot, F. Quéré, and R. Lopez-Martens, Phys. Rev. E **87**, 035101 (2013).
[14] H. Vincenti, S. Monchocé, S. Kahaly, P. Martin, and F. Quéré, Nat. Commun. **5**, 3403 (2014).
[15] A. Tarasevitch, *et al* Phys. Rev. Lett. **98**, 103902 (2007).
[16] S. Kahaly *et al.*, Phys. Rev. Lett. **110**, 175001 (2013).
[17] F. Dollar, *et al* Phys. Rev. Lett. **110**, 175002 (2013).
[18] M. Geissler, *et al* New J. Phys. **9**, (2007).
[19] B. Dromey, *et al* Phys. Rev. Lett. **102**, 225002 (2009).
[20] S. Chatziathanasiou,*et al.* Photonics **4**, 26 (2017).
[21] M. Reduzzi *et al.*, Journal of Electron Spectroscopy and Related Phenomena **204**, 257 (2015).
[22] Nomura,*et al.* Nat. Phys. **5** 124 (2009).
[23] R. Horlein,*et al.* New J. Phys. **12**, 043020 (2010).
[24] M. Yeung, *et al.* Phys. Rev. Lett. **110**, 165002 (2013).
[25] C. Bourassin-Bouchet, *et al.* Opt. Express **21**, 2506 (2013).
[26] H. Vincenti and F. Quéré, Phys. Rev. Lett. **108**, 113904 (2012).
[27] J. Wheeler, *et al.* Nat. Photonics **6**, 829 (2012).
[28] A. Leblanc, S. Monchocé, C. Bourassin-Bouchet, S. Kahaly, and F. Quéré, Nature Physics **12**, 301 (2016).
[29] J.-L. Vay, D. P. Grote, R. H. Cohen, and A. Friedman, Computational Science and Discovery **5**, 014019 (2012).
[30] H. Vincenti, M. Lobet, R. Lehe, R. Saskanka, and J-L. Vay, Computer Physics Communications **210** (2017).
[31] J.-L. Vay, I. Haber, and B. B. Godfrey, Journal of Computational Physics **243**, 260 (2013).
[32] M. Lewenstein, P. Salières, and A. L'Huillier, Phys. Rev. A **52**, 4747 (1995).
[33] F. Quéré *et al.*, Phys. Rev. Lett. **96**, 125004 (2006).
[34] F. Brunel, Phys. Rev. Lett. **59**, 52 (1987).
[35] A. Bourdier, Physics of Fluids **26**, 1804 (1983).
[36] P. Mercère *et al.*, Opt. Lett. **28**, 1534 (2003).
[37] S. Künzel *et al.*, Appl. Opt. **54**, 4745 (2015).
[38] J. M. Rodenburg *et al.*, Phys. Rev. Lett. **98**, 034801 (2007).
[39] P. Thibault *et al.*, Science **321**, 379 (2008).
[40] S. Monchocé *et al.*, Phys. Rev. Lett. **112**, 145008 (2014).
[41] See Supplemental Material, which includes Refs. [46–49], for more information on the experiment (part 1), the analytical models of harmonic phase curvature (part 2) , the comparison between experimental results and analytical models (part 3), and PIC simulations (part 4).
[42] K. Yee, IEEE Transactions on Antennas and Propagation

14, 302 (1966).

[43] M. Yeung, *et al* Nat. Photonics **11**, 32 (2016).

[44] A. Borot, *et al* Nat. Physics **8**, 416 (2012).

[45] P. Heissler, *et al* Phys. Rev. Lett. **108**, 235003 (2012).

[46] M. Bocoum, A. Vernier, A. Jullien, J. Faure, and R. Lopez-Martens, Optics Letters 40(**13**), 3009-3012

(2015).

[47] I. Haber, R. Lee, H. Klein, and J. Boris, Proc. Sixth Conf. on Num. Sim. Plasmas, Berkeley **8**, 4648 (1973).

[48] H. Vincenti, and J-L. Vay, Computer Physics Communications **20**, 147-167 (2016).

[49] G. Blaclard, H. Vincenti, R. Lehe, and J-L. Vay, ArXiv **arXiv:1608.05739** (2016).